HAL open science

Electric sampling of soot particles in spreading non-premixed flames: methodology and influence of gravity

Yutao Li, Antoine Bordino, Augustin Guibaud, David Montero, Jean-Marie Citerne, Jean-Louis Consalvi, Jose Torero, Guillaume Legros

To cite this version:

Yutao Li, Antoine Bordino, Augustin Guibaud, David Montero, Jean-Marie Citerne, et al.. Electric sampling of soot particles in spreading non-premixed flames: methodology and influence of gravity. Comptes Rendus. Mécanique, 2023, 351 (S2), pp.1-22. 10.5802/crmeca.182 . hal-04102189

HAL Id: hal-04102189

https://cnrs.hal.science/hal-04102189v1

Submitted on 22 May 2023

HAL is a multi-disciplinary open access archive for the deposit and dissemination of scientific research documents, whether they are published or not. The documents may come from teaching and research institutions in France or abroad, or from public or private research centers.

L'archive ouverte pluridisciplinaire **HAL**, est destinée au dépôt et à la diffusion de documents scientifiques de niveau recherche, publiés ou non, émanant des établissements d'enseignement et de recherche français ou étrangers, des laboratoires publics ou privés.

Distributed under a Creative Commons Attribution 4.0 International License

INSTITUT DE FRANCE
Académie des sciences

Comptes Rendus
Mécanique

Yutao Li, Antoine Bordino, Augustin Guibaud, David Montero, Jean-Marie Citerne, Jean-Louis Consalvi, Jose Torero and Guillaume Legros

Electric sampling of soot particles in spreading non-premixed flames: methodology and influence of gravity

Published online: 12 May 2023

https://doi.org/10.5802/crmeca.182

Part of Special Issue: Physical Science in Microgravity within the Thematic Group Fundamental and Applied Microgravity

Guest editors: Olga Budenkova (CNRS, Université Grenoble Alpes,Grenoble INP, SIMaP, 38000 Grenoble, France),
Catherine Colin (IMFT, Université de Toulouse, CNRS, INPT, UPS et GDR 2799 Micropesanteur Fondamentale et Appliquée) and Guillaume Legros (ICARE, CNRS UPR 3021, Univ. Orléans et GDR 2799 Micropesanteur Fondamentale et Appliquée)

This article is licensed under the
Creative Commons Attribution 4.0 International License.
http://creativecommons.org/licenses/by/4.0/

Les Comptes Rendus. Mécanique *sont membres du Centre Mersenne pour l'édition scientifique ouverte*
www.centre-mersenne.org
e-ISSN : 1873-7234

Comptes Rendus
Mécanique
Published online: 12 May 2023
https://doi.org/10.5802/crmeca.182

Physical Science in Microgravity within the Thematic Group Fundamental and Applied Microgravity / *Sciences physiques en microgravité au sein du GDR Micropesanteur Fondamentale et Appliquée*

Electric sampling of soot particles in spreading non-premixed flames: methodology and influence of gravity

Yutao Li*, [a], Antoine Bordino [b], Augustin Guibaud [c], David Montero [d], Jean-Marie Citerne [a], Jean-Louis Consalvi [e], Jose Torero [c] and Guillaume Legros [a, f]

[a] Institut Jean Le Rond d'Alembert/UMR CNRS 7190, Sorbonne Université, Paris F-75005, France

[b] Ecole Polytechnique, Palaiseau, France

[c] Department of Civil, Environmental and Geomatic Engineering, University College London, London WC1E6BT, UK

[d] Fédération de Chimie et Matériaux de Paris-Centre, Sorbonne Université, Paris F-75005, France

[e] Aix-Marseille Université, CNRS, IUSTI UMR 7343, 5 rue E. Fermi, 13013 Marseille, France

[f] CNRS-ICARE / Univ. Orléans, 1C Avenue de la Recherche Scientifique, 45071 Orléans Cedex 2, France

E-mails: yutao.li@sorbonne-universite.fr (Y. LI), antoine.bordino@polytechnique.edu (A. Bordino), a.guibaud@ucl.ac.uk (A. Guibaud), david.montero@sorbonne-universite.fr (D. Montero), jean-marie.citerne@sorbonne-universite.fr (J.-M. Citerne), jean-louis.consalvi@univ-amu.fr (J.-L. Consalvi), j.torero@ucl.ac.uk (J. Torero), guillaume.legros@sorbonne-universite.fr (G. Legros)

Abstract. Finer strategies of spacecraft fire mitigation require more experimental data related to fire detection. Fire detection systems developed on Earth rely massively on the optical detection of soot particles, which are present in the smoke. To detect the fire correctly, it is thus important to know how the optical properties of these particles are affected in reduced gravity. With different transport processes and increased residence time, soot in reduced gravity can be different from those produced at normal gravity. As their optical properties are related to their morphological properties, a better understanding about the evolution of soot particle morphology in flames under microgravity conditions is required. Within this context, a novel technique of soot sampling using electric field is applied to a spreading non-premixed flame at normal

* Corresponding author.

and micro-gravity. The soot particles sampled are observed subsequently under Transmission Electron Microscopy (TEM). Density, soot particle projected area, radius of gyration, fractal dimension, and primary particle size are extracted and the influence of gravity is investigated with the evolution of these morphological properties within the flame. Though the present study cannot be conclusive in itself, the similarity between the evolution of the optical density measured throughout the flame just before the electric perturbation required by the sampling technique and the evolution of the amount of soot deposited due to the electric perturbation along the sampling plates supports the future works that need to be devoted to further assess the consistency of the technique.

Keywords. Flame spread, Microgravity, Soot sampling, Soot morphology, Fire safety.

Funding. The authors feel grateful to the Centre National d'Etudes Spatiales (CNES) for its financial support under Contract No. 130615.

Electronic supplementary material. Supplementary material for this article is supplied as a separate archive available from the journal's website under article's URL or from the author.

Published online: 12 May 2023

1. Introduction

Fire safety is a major concern for space exploration [1]. As spaceflights transition from Low Earth Orbit (LEO) to deep space exploration, additional constraints challenge existing tools and protocols [2]. At the heart of the fire safety strategy, detection devices rely heavily on the detection of smoke produced by a fire-like diffusion flame. Discrimination from airborne dust is carried out through measurement of the scattering or ionization properties of soot particles, which are aggregates of impure carbon particles resulting from the incomplete combustion of hydrocarbons. However, little is known regarding the effect of reduced buoyancy flows on the soot particles' morphology and properties. Consequently, the investigation of smoke generated in a non-premixed flame in microgravity is crucial to prevent false alarms or, worse, the absence of alarm in a fire situation. In addition to these practical considerations, the tracking of soot particle formation, growth, and oxidation in reduced buoyancy presents fundamental benefits as these mechanisms can be captured with an elongated residence time, creating a new benchmark for numerical and theoretical models.

All existing smoke detectors on the International Space Station (ISS) today are designed and calibrated based on fire data from normal gravity experiments [3, 4]. The lack of data from microgravity experiments has led to detection accuracy difficulties. Trying to capture a fire signature as early as possible, Meyer et al. [5] analyzed particles generated in oxidative pyrolysis in microgravity and found that the particle dimensions were not significantly affected. However, this conclusion on oxidative pyrolysis contrasts with earlier findings regarding the size and morphology of soot particles produced in diffusion flames in microgravity. Due to the increase in residence time, more mature particles are retrieved and this makes the detection of fully-developed fire scenarios increasingly complex [6, 7]. Since the current smoke detectors on the ISS are based on light scattering, an investigation specific to the impact of gravity level on soot optical properties would be particularly relevant. The optimal situation is to perform straightforward measurements of soot particles using light scattering. However, microgravity soot particles suitable for investigation are difficult to generate. In addition, with space constraints in microgravity conditions, adding light scattering measurement equipment to experimental setups that produce soot particles is not easy. Therefore, studying the morphology of soot particles produced under microgravity can optimize the detection of soot particles by extracting their optical properties.

Non-intrusive optical techniques are available to investigate soot particle formation and evolution in situ without disturbing the flame. Such methods as Spectral Soot Emission (SSE) techniques [8], Laser-Induced Incandescence (LII) [9], light extinction [10], and light scattering [11] can lead to the evaluation of soot volume fraction, soot temperature, particle size, and aggregate morphology. Nevertheless, few optical techniques have been applied to flames in microgravity to study soot particle formation due to the constraints in equipment, timing, and volume. Reimann and Will [12] successfully applied the LII method to the study of soot formation in non-buoyant laminar jet diffusion flames in a drop tower experiment. Two-dimensional information on soot concentration and primary particle size in microgravity was obtained simultaneously, and the temperature field was measured by a 2-color emission pyrometer. It was shown that soot formation and oxidation change dramatically in microgravity, with the maximum flame temperature decreasing in the absence of buoyancy and the primary particle size doubling. Using another drop tower facility, Fujita and Ito [13] observed the soot agglomeration process in a jet diffusion flame using the Laser shadow method to evaluate the soot aggregates diameter and soot volume fraction. The size of soot aggregates was found to be much larger than that of a normal gravity flame, with the maximum size exceeding 100 μm. The size of soot agglomerates naturally increased with the distance from the burner outlet, following aging. It is likely that aggregates forming in such conditions can be conceived as aggregates of aggregates and show a hybrid-fractal character [14]. Such aggregates are called super-aggregates, and they exhibit multiple fractal dimensions. Considering the specificity of this soot particle morphology, there may be discrepancies between the real radiative properties of these particles and those calculated by simple, commonly used approximate light scattering models [15]. More recently, Guibaud et al. applied the implementation of the broadband modulated absorption/emission (B-MAE) technique to provide a mapping of soot temperature and volume fraction in a spreading flame during parabolic flights [16, 17]. These authors showed that the flow conditions, namely oxygen content, flow rate, and ambient pressure, affect the spreading rate and soot formation rate with dominant effects of oxygen content followed by pressure. However, this technique relies on particle size hypotheses regarding the dimensions of soot particles which the present study shows to be too limiting. All of these optical techniques are based on approximations regarding the optical properties of a soot-loaded atmosphere. Among the simplest absorption and diffusion assumptions commonly implemented, the Rayleigh approximation of the Mie theory provides simple calculations if the wavelength of the incoming light source is much larger than the particle size investigated. In typical flame conditions, the young soot particles as primary particles are near spherical with a size much smaller than the visible or near-infrared wavelength and they barely interact with each other. Therefore, they can be considered to be in the Rayleigh scattering approximation [18]. However, the mature soot particles as aggregates are usually beyond this limit in terms of dimensions and interactions, and other theories such as the Rayleigh–Debye–Gans for fractal aggregates (RDG-FA) approximation [18, 19] are better fit to the measurements. In microgravity, mature soot particles acting as microscopic fractal aggregates are more readily produced, casting doubt on the relevance of a Rayleigh approximation and supporting more elaborate assumptions. However, RDG and RDG-FA require additional information regarding the size, morphology, and fractal characteristics of the studied soot aggregates. Direct sampling of soot particles to collect data is then required to support the further development of optical diagnostics in reduced buoyancy environments.

To that end, Dobbins and Megaridis [20] implemented a thermophoretic sampling technique, now widely used to study the evolution of soot morphology and soot volume fraction in laminar diffusion flames [21–23]. In microgravity, Ku et al. [6] and Konsur et al. [24] performed the first thermophoretic sampling on a laminar diffusion flame in a drop tower experiment and analyzed the primary particle size and aggregate dimension with a Transmission Electron Microscope

(TEM). It was found that a longer residence time in microgravity enhanced soot formation and growth with an average primary particle size twice as large as that observed for soot formed at normal gravity. Following experiments aboard the space shuttle, Urban et al. [25] also performed soot sampling with the thermophoretic technique for laminar diffusion flame and outlined that soot primary particle size increases with distance from the burner, and that increasing ambient pressure tends to increase particle size. Although the results of the study using thermophoretic sampling in microgravity provide important and useful information about the morphology of soot collected in laminar diffusion flames, this sampling method is not fitted to spreading flames. The spreading flame over a solid fuel is a configuration closer to the real fire scenario. As the flame is always in movement, the thermophoretic sampling technique is difficult to apply in such a configuration. In addition, adding this sampling method requires adding quite a few additional devices, which is more difficult to implement in space-constrained microgravity experiments. Therefore, a special sampling technique is needed to study the soot particles formed by spreading flames in microgravity and to analyze their morphology.

To address this challenge, the present paper describes a novel particle sampling method that uses an electric field to sample soot particles on a brass plate both at normal and micro-gravity from a flame spreading on a cylindrical sample in an opposed-flow configuration. Introducing spatial resolution along the sample's axis, the evolution of soot particle morphology is tracked. Combining the ambitions of improving measurements from non-invasive optical diagnostics with the need to qualify the response of fire detection systems to soot particles being emitted at the trailing edge of the flame, the sampled soot particles are observed directly under a TEM and their morphological properties, namely density, particle projected area, radius of gyration, fractal dimension, and primary particles size distribution are extracted.

2. Initial observations and associated issues

Experiments have been conducted in microgravity and at normal gravity following the procedure detailed in Section 3, to highlight the effect of the gravity level on the flame from both macroscopic and microscopic perspectives. A diluted oxidizer stream consisting of 21% oxygen and 79% nitrogen flows at a rate of 150 mm/s in a combustion chamber, at an ambient pressure of 101.3kPa. Cylindrical wires, which consist of a 0.5 mm diameter Nickel-Chrome (NiCr) core coated with a 0.3 mm thick layer of Low-Density PolyEthylene (LDPE), are ignited under microgravity and normal gravity conditions, respectively. Once the flame is established, it propagates in an opposed flow configuration, as shown in Figure 1.

It can be seen that the gravity level impacts the condensed phase topology and the flame appearance at a macroscopic scale. In microgravity, the molten LDPE coating forms an axisymmetric bulb which pyrolyses at the flame leading edge upon heating from the flame (see Figure 1 (a)). At normal gravity, this bulb drips away on one side of the wire under its own weight (see Figure 1 (b)), affecting the spread rate, the pyrolysis, and breaking the symmetry of the flow to a certain extent. Furthermore, the flame is more stretched at normal gravity because of natural convection that accelerates the flow in the vicinity of the flame. In turn, this reduces the fuel residence time as compared to microgravity, according to the estimated characteristic flow time scale for the soot production in Section 4.1. This also affects soot formation, growth, oxidation, and radiative properties, and consequently changes the flame temperature and luminosity. The impact is such that the relatively slow flow conditions studied can lead to radiative quenching in microgravity, which is not observed at normal gravity.

These macroscopic observations have been documented in previous publications, using optical techniques that yield the fields of soot volume fraction and temperature. Yet, these quantitative measurements rely on a range of hypotheses regarding soot particles' dimensions and

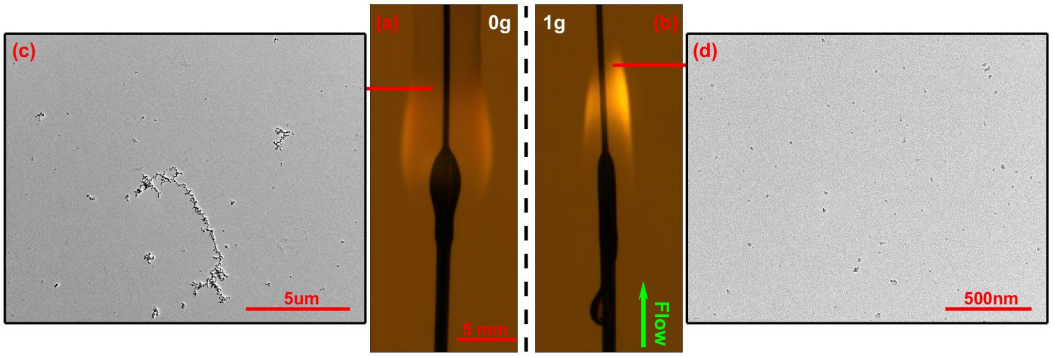

Figure 1. Illustration of the gravitational level impact on the flame appearance and the morphology of some soot particles sampled: (a)-(c) in microgravity; and (b)-(d) at normal gravity. The approximate locations of the soot sampling are represented by the end of the straight red solid lines on the imaging of the spreading flames (a) and (b). The smoking flame in microgravity (a) features large mature soot aggregates (c), that cannot be observed on the sampling (d) collected in the brighter flame at normal gravity (b).

morphology to solve the radiative transfer equation across the flame [16]. To assess the validity of these hypotheses, microscopic observations under TEM of particles sampled at the flame trailing edge are displayed for both microgravity and normal gravity in Figure 1 (c) and (d), respectively. The sampling is performed thanks to a novel methodology based on soot particle polarity, which is thoroughly described in Section 3. It can be noticed that the longer residence time in microgravity produces soot particles orders of magnitude larger than those sampled at normal gravity, and the more mature aggregates have a richer topology. This discrepancy clearly affects the quantitative results obtained with an optical setup, and also supports evidence of the need to adapt smoke detectors to the particle generated in a reduced-gravity environment.

In the following, the new sampling methodology is described and its relevance analysed before the morphological evolution of soot particles along the flame axis at both gravity levels is presented. Density, soot particle area, radius of gyration, fractal dimension, and primary soot particle are investigated as key parameters. The influence of gravity on the flame signature can then be documented using the above morphological properties.

3. Sampling with electric field

3.1. *Experimental setup*

The soot sampling method presented for the first time in this article has been designed to equip the Detection of Ignition And Mitigation Onboard for Non-Damaged Spacecrafts (DIAMONDS) rig described in detail in Ref. [26]. DIAMONDS can be handled on the ground to conduct experiments at normal gravity and, more distinctively, it can be boarded to the Novespace A310 ZeroG aircraft that operates parabolic flights to conduct experiments in reduced gravity. Each parabola provides 22 seconds of reduced gravity, aiming at zero acceleration in the referential of the aircraft with g-jitters lower than 0.05 g_0 (where $g_0 = 9.81\ m \cdot s^{-2}$).

DIAMONDS is built around a pressurized cylindrical combustion chamber with an inner diameter of 190 mm. A laminar oxidizer stream flowing parallel to the chamber's axis is established with a set oxygen content, pressure, and flow velocity within the ranges 0-21% in volume fraction, 50-150 kPa, and 0-300 mm/s, respectively. In the following, the conditions are set to 21%

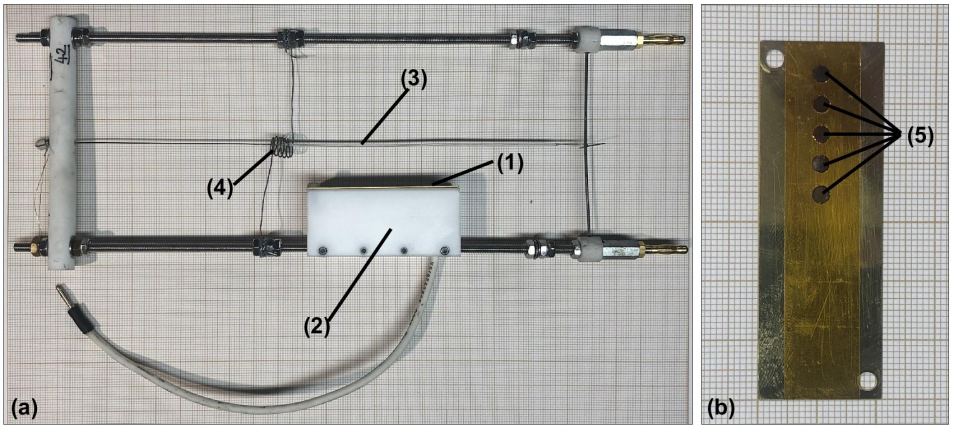

Figure 2. (a) Sample holder equipped with a brass plate (1). The brass plate is screwed to a PTFE beam (2) attached along the lower threaded rod of the sample holder. High voltage between the back of the plate and the NiCr core of the LDPE coated wire (3) that is connected to the threaded rod is supplied via a pin plug. The igniting Kanthal wire (4) can be seen; (b) Brass plate with TEM grids (5). The TEM grids are stuck to the plate with high-temperature adhesive tape.

oxygen content, 101.3 kPa and 150 mm/s. 150 mm-long NiCr-LDPE samples are attached on a sample holder along the chamber's axis, as illustrated in Figure 2 (a). Ignition, using an incandescent khantal wire rolled around the sample, can be controlled remotely once steady flow conditions are obtained to study flame spread. Depending on the position of the igniter, the flame can then spread with or against the flow. It has been reported that the flame could spread at a steady rate at both gravity levels under a wide range of counter-flow conditions [16, 17, 27, 28], while concurrent flame spread would continuously accelerate at normal gravity. As a result, this paper focuses on opposed-flow flame spread, and the igniter is located at the downstream edge of the sample.

The soot sampling technique relies on the electric field. With the help of the electric field, it is possible to manipulate the charged species in the flame. The most pronounced effect is the repeated collisions of ions with neighbouring neutral gases leading to a bulk fluid motion called ionic wind [29, 30], which has been evidenced under microgravity conditions [31]. Moreover, this conclusion was likewise verified under numerical models [32, 33]. The field of set amplitude and duration is generated between the metallic wire core, and a brass plate embedded into a PolyTetraFluoroEthylene (PTFE) beam, parallel to the wire and located 20 mm away from its axis. The boundary layer generated by the introduction of this additional element in the chamber can affect the flow downstream, but its action on the facing flame is limited. Assuming that the laminar boundary layer flow along the flat plate behaves according to the Blasius solution conditions, the thickness of the layer between the plate and the wire remains below 10 mm [34]. This is confirmed by observations of the unperturbed flame geometry, as shown in Figure 3 (a). The back of the brass plate is connected via a high voltage wire to an EMCO Q series DC high voltage generator located outside the combustion chamber. This device creates a tension up to 3 kV between the brass plate and the metallic core of the sample, which is electrically connected to the structure of the setup and acts as ground. The tension can be set for a duration prescribed by the operator. As the brass plate is charged by the generator, an electric field orthogonal to the sample's axis is generated between the brass plate, acting as the cathode, and the metallic

core, acting as the anode. The negatively charged particles of the flame caught in the field move towards the surface of the brass plate, creating an ionic wind rich in unoxidized soot particles. The particles then impact the surface of the brass plate, creating a shadow of the original flame. Similar to traditional thermophoretic sampling, the cold surface of the brass plate (compared to hot gas from the flame) serves an important purpose which is that it freezes heterogeneous reactions of the particles that are already captured. This chemical freezing action prevents changes in the soot morphology after the particles have impacted upon the cold surface [20].

The particles cannot be directly observed on the brass plate using TEM. To prevent the surface transfer and the associated degradation of the carbonaceous particles, TEM grids with a diameter of 3.05 mm are directly mounted on the central axis of the brass plate using high-temperature adhesive tape as shown in Figure 1 (b). The selected TEM grid is a copper grid with 300 square meshes covered with a film made of 5-6 nm pure carbon deposited on one side of the grid. These mesh grids have specific markers designed for quadrant location, including an asymmetrical mark in the rim and a center mark. It allows to identify their orientation at the time of the experiment and thus track the morphological evolution of soot particles at different positions along the vertical direction of the brass plate (see Figure 2 (b)). During the electric field activation, the particles are consequently deposited directly on the grids which can be detached with fine reverse action tweezers post-flight and brought to TEM for observation. Following observations from previous experiments in microgravity, five grids are regularly spaced from the top of the brass plate, with an inter-grid distance of 2mm.

Finally, all experiments are recorded by a JAI AT-140CL digital 12-bit tri-CCD camera equipped with a telecentric lens to limit the light collection to beams parallel to the optical axis. The camera images the spread at a rate of 39.06 fps on three 512x1396 pixel^2 CCD arrays, one for each of the broad green, blue, and red spectral bands. The resolution of the projected data is 72.6μm/pixel. A uniform backlighting consisting of a set of adjustable RGBW LEDs is alternately turned on and off as triggered by a pulse generator that also controls the camera acquisition. Doing so, a frame with backlighting follows one without. This strategy allows the effect of the soot sampling process on both the condensed coating and the smoke emissions to be captured.

3.2. *Sampling procedure and parameters*

To collect the soot particles produced in the flame after steady state spread conditions are reached in microgravity, sampling is performed at least 20 seconds after the hot wire ignition begins. Ignition is initiated before microgravity conditions are attained, to optimize the amount of time available for in-flight observations. Steady flame spread is defined as a situation where the flame front position progresses linearly, and the flame length and molten bulb volume are constant [35]. To capture particles from a range of positions within the flame, the electric field is generated once the flame faces the area covered by the TEM grids, which is indicated by horizontal lines on the visualization software to help the operator. Sampling onset is controlled manually because the flame spread rate varies based on the ambient condition.

The sampling sequence in microgravity is recorded in real-time by the tri-CCD camera images as shown in Figure 3 (a), (b) and (c), so the operator can track the evolution of the position of the flame relative to the brass plate. The positions of the five TEM grids are represented in yellow in the figure, and the dotted lines illustrate the upstream deformation position of LDPE, which can be assumed to correspond to the position where the solid fuel begins to pyrolyze and provide gaseous fuel.

During sampling (Figure 3 (b)), it can be noticed that the incandescent soot particles located within the flame and cold soot particles escaping from the trailing edge of the flame accelerate towards the brass plate immediately after the voltage is applied. At this point, it can be observed

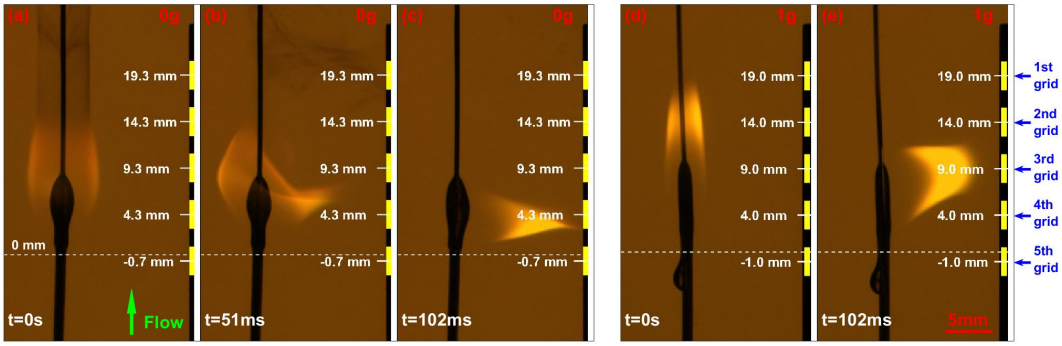

Figure 3. Sampling sequence in microgravity and normal gravity. The gravitational level is shown on the top right of the image and every TEM grid position is presented with a yellow rectangle. The horizontal dashed line indicates the upstream position of the LDPE deformation, which is set to z=0 mm (assumed to correspond to the position where the solid fuel begins to pyrolyze and provide gaseous fuel). The central position of each TEM grid along the vertical streamwise z-axis is then indicated with this origin as a reference. (a) and (d) are the last images before applying an electric field with t=0. (c) and (e) show maximal flame blending position under an electric field. (b) indicates how soot particles are moving toward the brass plate at the beginning of the sampling.

that soot particles in the gas phase move towards the nearest point on the brass plate. As such, one is inclined to anticipate that the position of the particles on the brass plate is tightly related to their initial position in the flame. As long as the electric field is sustained, the flame deforms towards the metal plate, as shown in Figure 3 (c). The flow rate appears to have a limited effect on the geometry of the flame, indicating that the ionic wind dominates the flow locally. The bright yellow aspect of the flame proves that soot particles are still generated when the voltage is on. It can be expected that soot particles produced in the presence of an electric field undergo a very different aging process compared to those collected in the initial sequence. It is also worth mentioning that the molten droplets are subjected to ionic forces and start to deform, with some spots of amorphous plastics being recorded on the TEM grids.

Voltage value and sampling duration are set in advance before each parabola flight. For effective sampling, it is necessary to ensure that sufficient soot can be collected on the TEM grids and that the quantity of soot particles is not too high to affect the subsequent TEM observation. From Figure 3 (b), it is found that at 51 ms after the application of the electric field, the soot to be sampled is still moving toward the brass plate, and the flame bends to the lowest point at 102 ms. Therefore, the sampling time should be at least 100 ms, so that the soot particles of interest have enough time to reach the brass plate. To ensure that enough soot can be sampled into the TEM grids, different sampling times of 100 ms, 300 ms, and 500 ms were investigated in microgravity under the same ambient conditions. It was observed that the soot particles on the TEM grid were already so dense at 300 ms that the amount of overlap prevented a straightforward analysis of the size and properties distribution, with more than 65% of the grid surface being covered by soot particles (versus 30% for a sampling period of 100 ms). A low sampling time of 100 ms is also preferred to minimize the amount of soot particles generated and aged in the electric field being sampled.

To minimize aging as the soot particles transit from their original location to the surface of the TEM grids, the particles should reach the brass plate as fast as possible. Three different voltage levels of 1.8 kV, 2.3 kV and 2.8 kV were carried out in microgravity with the same ambient

conditions. In the presence of a flow perpendicular to the sampling direction, the maximum bending angle of the flame was found to vary with the imposed voltage. The bending angles perpendicular to the flow direction were measured to be 18.1°, 7.1° and 4.8°, respectively. From the variation in the bending angle of the flame, it can be inferred that the flame bending is affected by both the ionic force generated by the voltage and the forced flow. The ionic force increases with the applied voltage and also increases the dominance of the ionic force against the forced flow. Meanwhile, it also appears that the particle sampling could be affected by the forced flow as particles move in the downstream region during sampling. In order to reduce this effect and let the particles reach the brass plate faster, the sampling voltage used in this paper is 2.8 kV.

At normal gravity, soot sampling relies on the same sampling parameters as in microgravity. Though there is no time constraint similar to parabolic flight, the flame cannot reach a steady state spread because of dripping. Soot sampling is then triggered when the flame passes the TEM grids to match the sampling position adopted in microgravity. As shown in Figure 3 (c) and (b), the spreading flame also bends toward the brass plat under the attracting electric field. However, due to the effect of natural buoyancy force, the bending is not as strong as in microgravity and reaches a maximum bending angle of 10.5°. The difference can be used to evaluate the force of the ionic wind and estimate the trajectory of the sampled soot particles.

The characteristic buoyancy-driven convective flow at normal gravity is provided by the momentum equation as:

$$U_{buoyancy} \approx \left(\frac{\triangle\rho}{\rho} gL\right)^{1/2} \tag{1}$$

where the density differences and the ambient density, $\triangle\rho$ and ρ respectively, can be considered to be similar [36]. At normal gravity, $g = 9.8\text{m}/s^2$ and a reported flame length $L_{f,1g} = 10.5$ mm give a buoyant flow velocity of 320 mm/s. Contrasting this value with the imposed forced flow of 150 mm/s in the combustion chamber, it can be concluded that the mixed convective flow velocity at normal gravity is then three times higher than it is in microgravity. Through the flame bending angle at different gravitational levels, it is possible to deduce the applied ionic force during the sampling. With the Boussinesq approximation, the natural buoyancy force can be determined by the following equation:

$$F_{buoyancy} = -g_0 \beta \rho_\infty (T - T_\infty) \tag{2}$$

Where T and T_∞ are the adiabatic flame temperature and the ambient temperature, respectively. With Gay-Lussac's law, the thermal expansion coefficient can be estimated as $\beta = 1/T$. As the flame bending angle is caused by forced flow, buoyant flow, and electric field, a simple force balance with the known buoyant force leads to an ionic force of $10.1 N/m^3$ during the 2.8 kV sampling.

With the same sampling voltage and duration, the sampling process at 1g is affected by natural convection, resulting in soot particles escaping from the flame to the brass plate with a different trajectory than under microgravity. Therefore, to investigate the influence of gravity levels on sooting properties, the following comparison is based on the overall evolution of different soot particle morphological properties along the flame axis, rather than a point-to-point comparison.

3.3. *TEM image acquisition*

The soot particles sampled on the TEM grids are observed under a JEOL JEM 1011 TEM, which is a tungsten hairpin 100kV electron microscope. The bright field images are acquired as tiff files on a CCD camera Gatan Orius SC 1000 A1 in 2672x4008 $pixel^2$. During observation, it is noticed

sample modification under electron beam revealed at least by soot vibration which limited the time of observation.

To follow the evolution of soot particle morphology along the wire axis, microscopic observations are performed at three positions on each grid. These three positions correspond to the central mesh and the two extreme meshes along the central axis. Since the sampled soot particles sizes fluctuate dramatically with the gravity level and the location of the observed grid position along the flame axis, the magnification of interest for the TEM observations varies accordingly from x400 to x60 000. The particles sampled at normal gravity cannot be observed at low magnification because their size is too small, while the massive soot aggregates collected in microgravity cannot be fully displayed at high magnification due to their excessive size. As a result, analyses are conducted over a range of magnifications.

In TEM, the observation range can be divided into low magnification below a x1200 magnification, and high magnification above. In the low magnification range, x400 images can show an entire mesh. It is used to verify whether the mesh has been damaged and whether the mesh is overloaded with soot particles. Also, it allows the quantitative analysis of the largest aggregates. A x1200 magnification can provide information about the aggregates that are too large to be fully visualized in the higher magnification images. At x5000 magnification, the particles generated at normal gravity begin to be clearly observed so that the images at this magnification can be applied to extract information on density, aggregate size, and certain large primary particle size, and to analyze the effects of gravity. The magnification between x5000 and x60 000 is then intended to extract information on primary particles.

4. Morphological properties analysis and discussion

As with all intrusive techniques, the samples are affected by the method used. The addition of an electric field to the flame can result in the inhibition or promotion of soot formation, and can alter the characteristics of soot deposition depending on the configuration of the experiment. Xie et al. [37] investigated the effect of direct and alternating current on soot formation for diffusion counter-current type flames. It was found that the residence time of charged soot precursors and charged soot particles in the flame could be altered by electric fields, which led to the large changes in soot formation observed in the experiments. In addition, Weinberg et al. [38] found that the electric field also modified the flow of charged species thus affecting the number of soot particles that acquired charge through the diffusion mechanism. Thus, both the size and the number of soot particles can be affected by the electric field. It is also important to consider that, if the suggestion about the cyclic participation of ions in the formation of PAHs and crystallites is correct, the ion pathway for soot formation is not excluded when soot sampling in an electric field [39, 40]. The above studies all show that the application of electric fields to flames is likely to have an impact on soot particle formation. Hence, the present soot sampling technique may affect soot formation.

In order to discriminate the investigated effect of gravity on soot particles from the unwanted effect of electric field on soot particles, the corresponding characteristic time needs to be appreciated. Different gravity level affects the natural convection and thus the soot residence time, and this characteristic flow time scale of the soot production process can be estimated as:

$$t_{res,s} \sim \frac{L_f}{u_\infty} \tag{3}$$

where u_∞ is the mixed convective flow velocity which includes the buoyant flow velocity and the forced flow velocity, and L_f is the visible flame length. The visible flame length in microgravity is $L_{f,0g}$ = 11.3 mm, hence its flow residence time for soot production is estimated as 75.5 ms.

In contrast, the residence time is 22.3 ms at normal gravity. Alternatively, it can be observed from Figure 3 (b) and (c) that the soot is moving toward the brass plate 51 ms after the activation of the electric field, while the flame is completely bent at t=102 ms. Therefore, the soot particles need to be fully collected in the time between 51 ms and 102 ms. Since the actual sampling time is not much smaller than the soot particle residence time for both gravity levels, it is likely that the electric field during the sampling process has an effect on soot particle formation for all sampling positions. As mentioned in Section 3.2, the flame is bent and pointed to the 3rd (normal gravity) and 4th (microgravity) grid sampling positions, respectively, due to the electric field. These positions are more severely affected by the electric field than the other sampling positions. The electric field is applied for a set time and these positions are affected by the bent flame for a longer time. As a result, the grids located at these positions are likely to collect more soot particles formed under the influence of the electric field.

As a result, the sampled soot particles are generated by the competition between the electric field force and buoyancy force, and the following discussion on the TEM measurements cannot directly conclude the sole effect between normal and micro-gravity. Since the sampling conditions (sampling voltage and sampling duration) applied at both gravity levels are the same, gravity remains the only variable in both cases. The discussion related to the effect of gravity on soot particles can still be carried out but in the context of the transient presence of the electric field. As the electric field is applied to the entire flame during the sampling process, it affects the overall generated soot particles in the flame under the same duration. To extract the influence of gravity on soot particles, it would be better to use the evolution of morphological soot particle properties along the flame axis through the comparison of the results obtained at normal and micro-gravity.

4.1. *Density of soot particle projected area*

With TEM images, the most intuitive results are the two-dimensional density of soot particles on the image and the projected area of each individual soot particle contributing to this density. As a result, the sampling procedure is designed as a trade-off between the need of statistical consistency, i.e. a significant number of particles sampled, and that of discrimination among the particles observed, i.e. a weak overlapping among the particles' projected area.

To extract the information on the density of soot particles on the image and the projected area of each individual soot particle, it is necessary to accurately identify the soot particles on the TEM images. The method of soot segmentation proposed by Sipkens and Rogak [41] is applied, which is built around a k-means clustering algorithm, and involves multiple steps of pre- and post-processing to denoise the images, enhance contrasts, and reconstruct the shapes of particles once the images have been binarized. This segmentation method has proven robust across almost all images, with a few cases of failures where the algorithm is unable to identify particles, due to the image being too noisy (which happened mainly with low magnification 1g-sampling images, where particles sizes rarely exceed a dozen pixels). In these latter cases, binarization was performed manually, while keeping the same image pre- and post-processing. In comparison, the Otsu thresholding method was much less efficient and tended to underestimate the binarization threshold, which led to aggregates being split into multiple parts. The k-means clustering tends on the other hand to overestimate this threshold a little, overestimating the area-equivalent diameter of individual aggregates by 2% on average [41]. With the generated binary masks, the density of soot particles is computed as the ratio of the total area of soot particles to the total area of the image and the individual soot particle projected area can be also obtained easily with the summation of all the detected areas for individual soot particle.

Figure 4 (a) shows the evolution of soot particles' projected area density over the grid observed by TEM as a function of the grid's position along the streamwise z-axis at both gravity levels. In

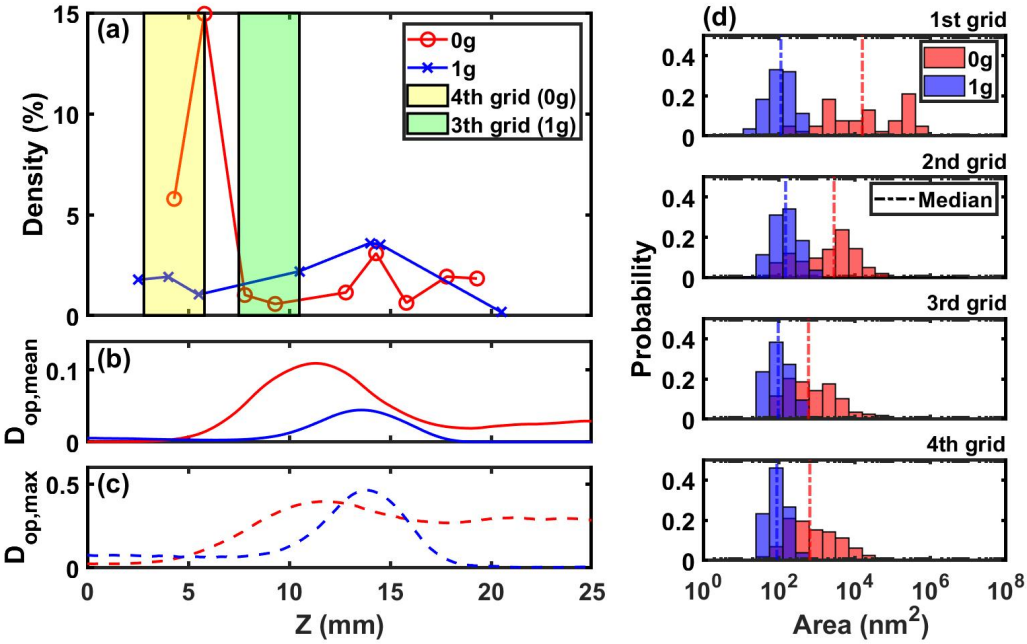

Figure 4. (a) Evolution along the streamwise coordinate z of the soot particle density over the sampling grid observed by TEM. The yellow and the green shaded areas indicate the 4th grid in microgravity and the 3rd grid in normal gravity, respectively. These areas represent the positions where the sampling is strongly impacted by the electric field. The corresponding positions of the different grids are also shown in Figure 3. (b) and (c) Evolutions with z of the mean and maximum optical density measured through the flame just before the electric perturbation and the subsequent sampling. (d) Distribution of the sampled soot particle's projected area over every grid.

microgravity, it can be noted that the density of the 4th grid is much higher than that of the other positions. From Figure 3 (c), it can be found that the flame bent and pointed to the 4th grid under the influence of the electric field. As described in Section 3.2 and at the beginning of Section 4, during the presence of the electric field, the flame points to this 4th grid position and continues to produce soot particles that affect the results, leading to a higher density of particles deposited on the grid at this sampling position. Nevertheless, the results from the other positions can still provide useful information regarding the difference in soot particles obtained at normal gravity and microgravity. Ignoring the 4th grid, i.e. the region represented by the yellow shaded region on Figure 4 (a), it is observed that the density tends to increase then decrease when analyzing meshes on the grids facing the flame from the leading to the trailing edge. Finally, the density gets constant on meshes located beyond the smoke point, i.e. the flame trailing edge.

At normal gravity, a very similar influence of the flame bent due to the electric field is also reported. This time, the flame bends and points slightly downstream, i.e. to the 3rd grid due. This downstream shift can be attributed to the buoyant force (as shown in Figure 3 (e)). Overall, the soot density increases, then decreases, and finally vanishes with the grid positions. Observing the meshes on the grid closest to the flame leading edge, the soot density is higher than that in microgravity. Interestingly, this trend is reversed on the meshes of the grid when moving towards the flame trailing edge. This observation correlates with a heavy smoke release by the non-buoyant flame which cannot be observed at normal gravity (as shown in Figures 3 (a) and (d)).

It also means that the obtained results can be projected to some extent to the evolution of the soot properties along the flame just before the electric field is applied.

To further assess this later statement, the optical density of the spreading flame can be extracted and compared with the density of the sampled soot particles on the grids. In earlier investigations, Guibaud et al [35] showed that the fields of local soot temperature and volume fraction can be extracted from the imaging of the flame shown in Figure 3. These authors especially evidenced that for the surrounding flow conditions investigated here, the flame produces a higher peak local soot volume fraction at normal gravity but a higher overall soot loading in microgravity. This is mainly attributed to the thermal expansion that makes the flame's peak diameter wider in microgravity while the residence time is enhanced [42].

The raw information processed by the diagnostics set by Guibaud et al is the field of optical density throughout the flame. Within the spectral range covered by the imaging, this optical density is highly dominated by the absorption of light by the soot particles. That being said, the relationship between the morphological features of the soot particles and their propensity to absorb light is complex and depends on many factors (e.g., the size and distribution of the soot particles). This will not be discussed in detail in this paper. However, it is of interest to assess the correlation between the distribution of optical density within the flame before it is perturbed by the electric field and the evolution with the grid's position of the soot particles' projected area density on the grid.

In brief, the integrated optical density through the flame can be extracted using the image of the flame with backlight, the following one without backlight, the image only with backlight (i.e. without any flame), and the one with only background noise (i.e. without any flame and without any backlight). On any pixel, their corresponding intensities captured by the camera are referred to as $I^{fl,on}$, $I^{fl,off}$, $I^{backlight}$, and I^{noise}, respectively. Based on the above information, the integrated optical density of the flame D_{op} can be evaluated as follows:

$$D_{op} = -log\left(\frac{I^{fl,on} - I^{fl,off}}{I^{backlight} - I^{noise}}\right) \tag{4}$$

For both flames in microgravity and at normal gravity, the data are extracted just before the electric field is set (i.e., Figure 3 (a) and Figure 3 (d), respectively). Then, the evolution along the streamwise coordinate z of the optical density $D_{op,mean}$ averaged over the flame width can be obtained (see Figure 4 (b)), together with that of the peak optical density $D_{op,max}$ (see Figure 4 (c)). Ignoring the upstream regions affected by the impact of the flame on the brass plate during the sampling process, an encouraging similarity between the evolutions of the optical density within the flame and the density of the soot particle's projected area on the grid can be observed. For the flame at normal gravity, both the maximum and mean optical densities peak around z=15 mm so does the density of the soot particles' projected area on the grid. In addition, all these densities vanish beyond the flame's trailing edge (z≈18 mm). For the flame in microgravity, the peaks of optical density (z≈1 1mm) and projected area one (z≈14 mm) are more separated. It is worth mentioning here that the sampling procedure has been primarily designed to evaluate the morphological features of soot, which in turn leads to relatively low levels of soot particles' projected area density on the grid. Consequently, it might be not curious that the trends of density displayed on the grids cannot discriminate levels of $D_{op,max}$ ranging from 0.4 at z≈11 mm to 0.35 at z>17 mm in microgravity (see Figure 4 (c)). Still, the plateau of density beyond the smoke point (z>17 mm) shown by both $D_{op,max}$ and $D_{op,mean}$ looks to be captured also on the higher two grids (z=18 mm and z=19 mm).

Finally, at the trailing end of the flame, both sets of information, i.e. the sampling and the optical ones show a crossover of the trends between both gravity levels. At z=16 mm (see Figure 4 (c)), the peak optical density gets lower at normal gravity than in microgravity.

Thus, though the present study cannot be conclusive in itself, the significant fit of the aforementioned profiles in the direction of the streamwise coordinate z supports the relevance of the sampling technique. It appears that the evolution along the streamwise coordinate z of the features extracted from the soot particles sampled on the TEM grids can represent to some extent the evolution of these features along the flame height just before the electric field perturbed the flame.

The distribution of soot particle projected area is reported to analyse the evolution of the size of soot particles along the brass plate. It can be found that the median projected area of the soot particles sampled in microgravity is much larger than that of soot particles at normal gravity at all grid locations. In addition, they follow different trends along the flame axis. In microgravity, the median value gradually shifts to larger area values from the grids facing the flame leading edge to the grids facing the flame trailing edge. In comparison, the median projected area of the soot particles remains stable at normal gravity. Since the 4th grid is more severely affected by the electric field than the other sampling locations, particle area distribution is not further analysed. Starting from the 3rd grid, a log-normal distribution is reported. This log-normal distribution breaks down at the 2nd grid facing the trailing edge of the flame, where a higher number of large particles is reported forming a bimodal distribution. Observing the 1st grid, the largest particles are reported but no pattern can be extracted from the distribution. At normal gravity, the distribution does not vary much along the flame axis, and it always shows a log-normal type distribution. However, upon very careful observation and without considering the 3rd grid position which is severely affected by the electric field, from the median and the maximum value of the particle area, it can be noticed that the particle area tends to increase first and then decrease along the direction from the leading to the trailing edge of the flame. The increase in the projected area can be explained by the formation and growth of the soot particles and the decrease is likely due to oxidation as the normal gravity flame training edge [43, 44]. According to the TEM image observation, most of the particles sampled at normal gravity are spherical primary particles, which contrasts with the fractal-like aggregates reported in microgravity. This difference is related to the discrepancy in residence time at normal and micro-gravity, allowing soot to mature in the absence of buoyant flow. According to Eq. (1), the residence time in microgravity is three times larger than at normal gravity given that the corresponding mixed convective flow is three times lower. With a shorter residence time of soot production, the soot particles sampled at normal gravity do not have enough time to become more mature under high temperatures and lack oxygen conditions as in microgravity. And these young and small soot particles are readily oxidized after contact with oxygen at the trailing edge of the flame [45], hence, it is more difficult to have smoke emission at normal gravity than in microgravity.

4.2. *Radius of gyration and fractal dimension*

The radius of gyration, R_g, and fractal dimension, D_f, are key features that drive the optical properties of soot aggregates from particle morphology [18, 46]. Intrinsically, they are parameters that can describe the overall size of the particle and its structure. R_g represents the overall size of the aggregate, while D_f informs on the chain-like (low values of D_f) or densely packed spherical (high values of D_f) internal structure [47]. Both are important properties to select the most suitable approximation for optical diagnostics and numerical simulations. Using the binarized TEM images enables the analysis of the gyration radius and fractal dimension. The radius of gyration is determined using a centroid approach, as described in [48], where R_g is computed as the root mean square distance of all the mass elements of aggregate to its center of mass.

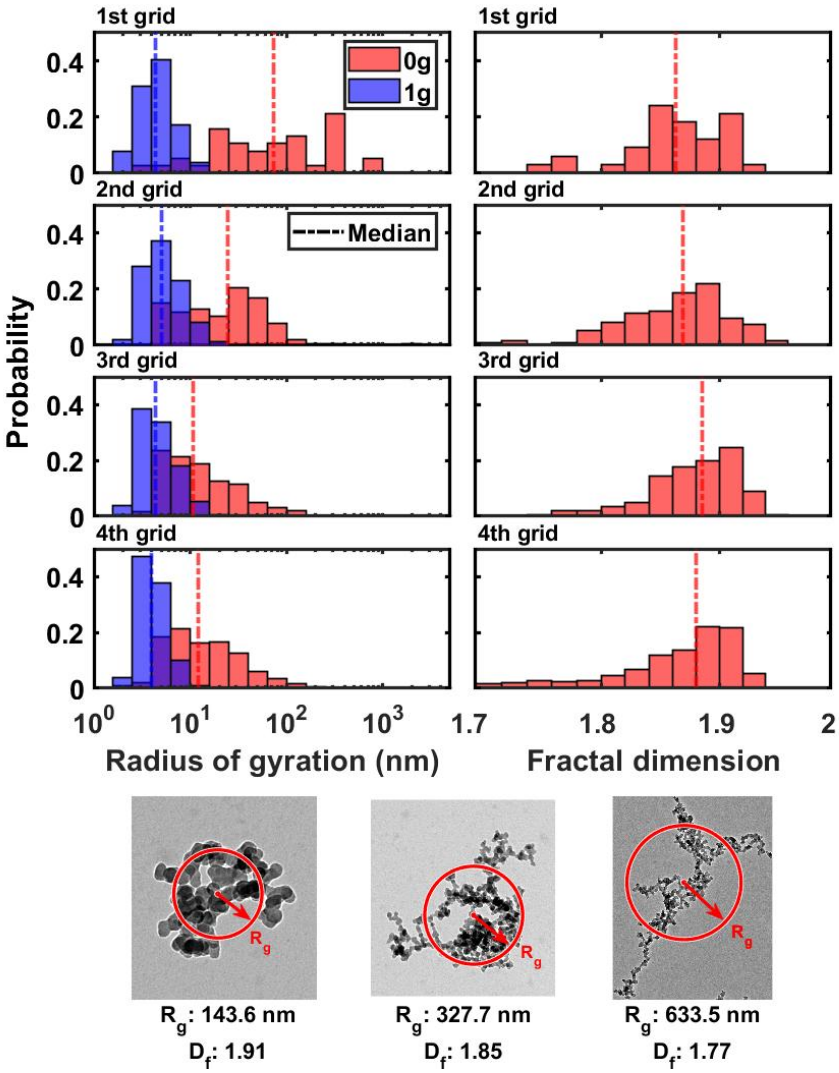

Figure 5. Evolution of radius of gyration distribution (left) and fractal dimension distribution (right), and three examples of the aggregates sampled with different radius of gyration and fractal dimension in microgravity (bottom).

The considered mass elements are the pixels composing the binary mask of the aggregate, each having a weight of 1. D_f is computed using a box counting method as:

$$D_f = -\lim_{a \to 0} \frac{ln(N(a))}{ln(a)} \tag{5}$$

where a represents the box size and $N(a)$ is the number of boxes needed to recover the aggregate binary mask. This method is limited by the resolution of TEM image [49]. If the studied soot particle takes up too few pixels, the precision drops as the range of potential box sizes is too limited. Therefore, only soot particles with a surface area above 500 pixels are analysed. According to the image resolution, particles with an area as small as 230 nm^2 can be processed.

Figure 5 shows the evolution of the radius of gyration and fractal dimension distribution along the brass plate. The radius of gyration follows the trend of the projected area distribution reported in Figure 4 at both gravity levels. R_g is much smaller at normal gravity than that in microgravity, with a median value remaining below 10 nm. In microgravity, soot particles sampled at each grid location can have much greater R_g, showcasing a median value as large if not larger than any of the particles sampled at normal gravity. Looking at particles on the 2nd grid which faces the trailing edge of the flame, the soot particles grow to a median size of 48 nm. This growth of the radius of gyration continues when processing the particles sampled on the 1st grid facing the smoke trail, which have a median size of 143 nm with a maximal size up to 695 nm. This evolution indicates that soot particles sampled in microgravity continue to mature and grow until they escape from the flame at the trailing edge of the flame. As mentioned previously, the soot particles are mainly small spherical primary particles at normal gravity. For those fractal-like soot aggregates in microgravity, the evolution of its structure can be tracked by the fractal dimension distribution. Overall, the mean value of the fractal dimension stays around 1.86 for all grids, but the distribution changes significantly. A more segregated distribution of fractal dimensions is reported in the 1st and 2nd grids, as shown in Figure 5. When following the sampling locations on the brass plate from the leading to the trailing edge of the flame, the median tends to move towards smaller fractal dimensions, which means that more particles transition to the chain-like branched aggregate. It is worth mentioning that the soot particles in the 4th grid, which are more severely affected by the electric field than the other sampling positions, display a different morphological structure and their distribution is more dispersed than on the other grids.

4.3. *Primary particle size distribution*

The purpose of the primary particle study is to identify the evolution of the primary particle size along the flame axis. Therefore, this necessarily leads to the development of a specific segmentation algorithm, which aims at identifying a majority of the primary particles. This allowed for faster treatment of a higher number of aggregates, which provided a good statistical correction to compensate for the missing particles.

This semi-automated method used three different features to segment primary particles. First, it makes use of the Circular Hough Transform (CHT) based algorithm, applied to the previously generated binary masks (as shown in Figure 6 (b)), to identify the particles on the contour of the aggregate (yellow circles on Figure 6 (a)). Then, the color gradients of the image are calculated to map all of the uniformly shaded areas of the aggregate which likely correspond to one primary particle (as shown in Figure 6 (c)). The center of each region is then computed and fed to the Center-Selected Edge Scoring (CSES) algorithm [50] which tries and fits a circle on the TEM image at this approximate location (blue circles in Figure 6 (a)). Finally, an entropy filter is applied to the image to highlight highly-textured areas (as shown in Figure 6 (d)), which are locations where a high number of overlapping particles is likely to be found, and the CSES algorithm is once again applied in this area to identify the primary particles (red circles on Figure 6 (a)).

This method is controlled by a set of operator-defined image-wide parameters, as experience showed that the optimal control parameters are the same for all aggregates in one TEM image. These parameters are:

- The particle radius range has to be adjusted when moving along the flame to accommodate for the evolution of soot maturity.
- The binarization threshold for both the gradient map and the entropy-filtered image mainly depends on the contrast and the overall quality of the image.

This method has given satisfying results on all images, both in microgravity and normal gravity, even though the gradient and entropy features require the aggregate to have a certain size to

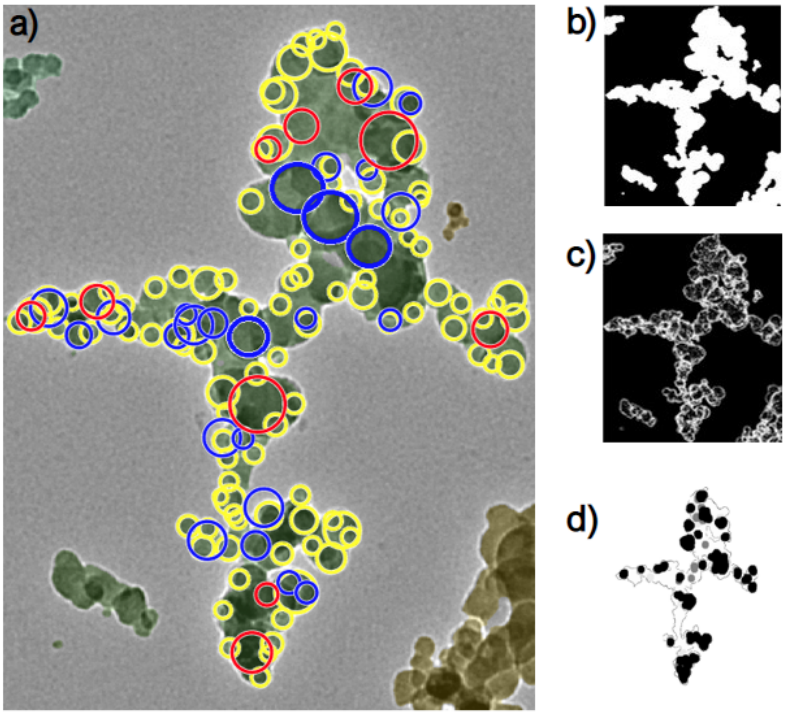

Figure 6. Primary particle segmentation process on one aggregate using three different features: (a) result of the primary particle segmentation, (b) binarization, (c) gradient map, and (d) entropy filtering.

be truly efficient. The number of segmented primary particles was at least 70% of the number of particles identified using an equivalent fully-manual method. The main limitations lie in the difficulty for the CSES algorithm to tell apart particles that overlap with a high number of others and to identify particles in large uniformly-shaded areas. Moreover, as it can be seen in Figure 6, a very small number of the drawn circles are erroneous, which requires manual cleaning. However, their influence on the overall measurements is negligible due to their statistically small number, and this problem is therefore a reasonable concession considering the great gain in efficiency of the method.

Figure 7 shows the evolution of the primary soot particle radius distribution along the flame axis at both gravity levels. Overall, the primary particles at normal gravity are smaller than those in microgravity and they are less than 10nm. This proximity to the radius of gyration of particles at normal gravity highlights the fact that the soot particles probed at normal gravity barely aggregate. Moving away from the grids closer to the flame leading edge, the primary particle size distribution at normal gravity shifts from a power-law to a log-normal type distribution and their size tends to increase first (2nd grid) and then decrease slightly (1st grid). In the beginning, the power-law type distribution is due to the particles nucleating and growing a radius between 2-4 nm [51]. As these particles continue to grow in the flame, their radius continues to grow to between 6-8 nm. At the grid position corresponding to the trailing edge of the flame, the distribution of soot primary particles is slightly skewed towards smaller particles because of the oxidation. In microgravity, the overall evolution of primary particle size distribution is very different from that in normal gravity and is more dispersed. The log-normal type distribution dominates from the 3rd grid position onward. The primary soot particle radius distribution on the

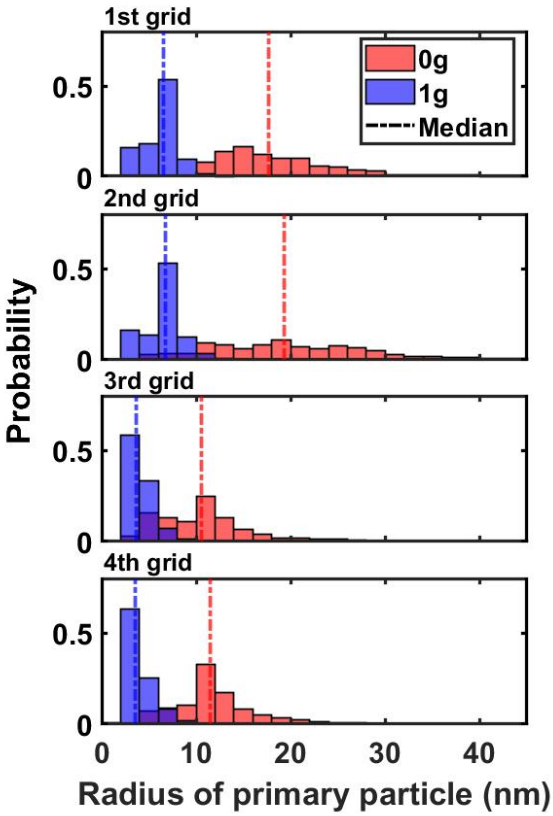

Figure 7. Evolution of primary particle radius distribution in microgravity and at normal gravity.

1st and 2nd grids facing the smoke-point transition are highly dispersed and the median particle size is larger than that on the 3rd and 4th grids facing the flame. However, a reduction in the median size of primary soot particles occurs between the 2nd and 1st grids, which is assumed to happen due to the oxidation process.

Going back to the investigation on optical approximations, the following size parameters need to be evaluated [18]:

$$x_p = \pi * d_{pp}/\lambda \tag{6}$$

where d_{pp} is the diameter of the primary particle and λ is the studied wavelength. It is commonly admitted that a value of x_p below 0.3 justifies the use of the Rayleigh limit of the Mie theory. In addition, another factor to be taken into account is the dispersion of the primary particle size, as the polydispersity of primary particles has been shown to play a significant effect on the radiative properties of soot [52–54]. Basically, the distribution of primary particle radius has a standard deviation between 15% and 25% of its mean value, which can be largely uniform depending on the particle size [55]. As has been emphasized previously, soot particles sampled using the sampling method presented in this paper are potentially affected to some extent by the electric field. Therefore, it is difficult to process soot particle morphological characteristics presented in this paper as absolute dimensions to validate any numerical model or the optical diagnostic method. However, the ambition of the present work is not to develop a new configuration that

could be supported by numerical endeavours trying to capture the complex action of the electric field on the spreading flame. Instead, the objective is to provide clues regarding how particle dimensions and morphology are affected by the absence of buoyant flow in a steady spread configuration. According to the primary particle radius obtained in the present work, the largest primary particle radius does not exceed 10nm at normal gravity, resulting in a $x_p < 0.3$ for the visible or near-infrared wavelength ($\lambda > 500$ nm). Yet, it can reach a maximum of 40 nm in microgravity, corresponding to an x_p of 0.5, as part of massive aggregates of a size similar to the wavelength of visible light. As such, it is reasonable to assume that individual primary particles approximate Rayleigh scattered particles at normal gravity but that this assumption fails in microgravity [55]. Yet, the standard deviation of the primary soot particle sampled at normal gravity for each grid is above 25% of its mean primary particle radius, raising questions about the impact of polydispersity on the measurements. In microgravity, the same standard deviation is higher than 30% of the mean value of radius for all the sampling positions, even reaching 51% at the 2nd grid. Hence, it could be anticipated that both its primary particle size and polydispersity pose a greater challenge than the case at normal gravity to estimate the optical properties [19].

5. Conclusion

The novel technique of soot sampling using an attracting electric field is applied to the flame spreading in an opposed flow over the LDPE coating of NiCr both at normal and microgravity. The main parameters of the sampling technique are the voltage applied and the time it is applied. Following the analysis, a shorter sampling time together with a higher sampling voltage lead to an appreciated trade-off between the need for visual discrimination among soot particles observed and the statistical consistency of the features extracted. The differences between microgravity and normal gravity sampling are identified as the experimental setup is operated at both gravity levels.

The sampled soot particles are observed under TEM. If the sampled soot particles are potentially affected by the electric field, keeping the sampling parameters constant under varying gravity field allows a relative investigation on the effect of buoyant flow on particles distributions. The effect of gravity on soot formation is explored by comparing the evolution of soot density, particle area, radius of gyration, fractal dimension and radius of primary particle at different locations of sampling grids located along the flame axis. In microgravity, the density of soot particles on grids facing the leading edge of the flame is lower than at normal gravity. Interestingly, this trend is reversed on grids facing the trailing edge of the flame, which correlates with a heavier smoke release reported for non-buoyant flames. Overall, soot particles sampled in microgravity are larger than those collected at normal gravity. In addition, the distributions of soot particle characteristics are different at both gravity levels: if a clear central peak can be identified at normal gravity, the distribution tends to be more complex in mircrogravity where increased dispersion is reported in the grids closer to the flame trailing edge. According to the TEM images, the soot particles sampled in microgravity show up as fractal-like aggregates while they are mainly spherical primary soot particles at normal gravity. The evolution of the soot aggregate structure in microgravity was tracked by its fractal dimension. According to the evolution of fractal dimension, the closer to the trailing edge of the flame, the more the soot tends to grow as chain-like branched aggregate. Looking then at the large and polydisperse primary particles sampled in microgravity, the limitation on the optical assumptions behind detection strategies of smoke detectors is highlighted. In contrast, particles sampled at normal gravity fall into the assumptions relevant to the Rayleigh limit of the Mie theory, as commonly implemented.

The present image-processing technique has potential for optimization, and further the 3-dimensional soot morphological properties could be obtained by electron tomography [56].

In addition, contrasting the present results with observations from other non-invasive experimental techniques [57, 58] or results from steady spread numerical simulations [27, 59] will refine the understanding of the effect of gravity on soot formation in spreading flames.

Conflicts of interest

The authors declare no competing financial interest.

Acknowledgments

The authors feel grateful to the Centre National d'Etudes Spatiales (CNES) for its financial support under Contract No. 130615. And the JEM1011 Microscope is part of FCMat, The Federation of Chemistry and Materials of Paris-Center (Sorbonne Université).

Supplementary data

Two videos of soot sampling in microgravity and at normal gravity, an original TEM image, and its results of primary particle size are provided as supplementary data.

References

[1] C. National Research, *Recapturing a Future for Space Exploration: Life and Physical Sciences Research for a New Era*, National Academies Press, 2011.

[2] A. Guibaud, G. Legros, J.-L. Consalvi, J. Torero, "Fire safety in spacecraft: Past incidents and Deep Space challenges", *Acta Astronaut.* **195** (2022), p. 344-354.

[3] R. Bukowski, G. W. Mulholland, *Smoke detector design and smoke properties. Volume 13*, National Bureau of Standards technical note, vol. 973, Department of Commerce, National Bureau of Standards, National Engineering Laboratory, Center for Fire Research, 1978.

[4] R. Bukowski, R. Peacock, J. Averill, T. Cleary, N. Bryner, P. Reneke, "Performance of Home Smoke Alarms, Analysis of the Response of Several Available Technologies in Residential Fire Settings", Tech. Report Technical Note (NIST TN) - 1455, National Institute of Standards and Technology, Gaithersburg, M.D., 2003.

[5] M. E. Meyer, D. L. Urban, G. W. Mulholland, V. Bryg, Z.-G. Yuan, G. A. Ruff, T. Cleary, J. Yang, "Evaluation of spacecraft smoke detector performance in the low-gravity environment", *Fire Saf. J.* **98** (2018), p. 74-81.

[6] J. C. Ku, D. W. Griffin, P. S. Greenberg, J. Roma, "Buoyancy-Induced Differences in Soot Morphology", *Combust. Flame* **102** (1995), no. 1, p. 216-218.

[7] H. Ito, O. Fujita, K. Ito, "Agglomeration of soot particles in diffusion flames under microgravity", *Combust. Flame* **99** (1994), no. 2, p. 363-370.

[8] M. Y. Choi, A. Hamins, G. W. Mulholland, T. Kashiwagi, "Simultaneous optical measurement of soot volume fraction and temperature in premixed flames", *Combust. Flame* **99** (1994), no. 1, p. 174-186.

[9] H. A. Michelsen, C. Schulz, G. J. Smallwood, S. Will, "Laser-induced incandescence: Particulate diagnostics for combustion, atmospheric, and industrial applications", *Prog. Energy Combust. Sci.* **51** (2015), p. 2-48.

[10] M. Y. Choi, G. W. Mulholland, A. Hamins, T. Kashiwagi, "Comparisons of the soot volume fraction using gravimetric and light extinction techniques", *Combust. Flame* **102** (1995), no. 1-2, p. 161-169.

[11] C. M. Sorensen, "Light Scattering by Fractal Aggregates: A Review", *Aerosol Sci. Technol.* **35** (2001), no. 2, p. 648-687.

[12] J. Reimann, S. Will, "Optical diagnostics on sooting laminar diffusion flames in microgravity", *Microgravity Sci. Technol.* **16** (2005), no. 1, p. 333-337.

[13] O. Fujita, K. Ito, "Observation of soot agglomeration process with aid of thermophoretic force in a microgravity jet diffusion flame", *Exp. Therm. Fluid Sci.* **26** (2002), no. 2-4, p. 305-311.

[14] W. Kim, C. M. Sorensen, D. Fry, A. Chakrabarti, "Soot aggregates, superaggregates and gel-like networks in laminar diffusion flames", *J. Aerosol Sci.* **37** (2006), no. 3, p. 386-401.

[15] R. Ceolato, L. Paulien, J. B. Maughan, C. M. Sorensen, M. J. Berg, "Radiative properties of soot fractal superaggregates including backscattering and depolarization", *J. Quant. Spectrosc. Radiat. Transfer* **247** (2020), article no. 106940.

[16] A. Guibaud, J.-M. Citerne, J.-L. Consalvi, G. Legros, "On the effects of opposed flow conditions on non-buoyant flames spreading over polyethylene-coated wires - Part 1: spread rate and soot production", *Combust. Flame* **221** (2020), p. 530-543.

[17] A. Guibaud, J.-M. Citerne, J.-L. Consalvi, G. Legros, "On the effects of opposed flow conditions on non-buoyant flames spreading over polyethylene-coated wires - Part 2: soot oxidation quenching and smoke release", *Combust. Flame* **221** (2020), p. 544-551.

[18] Ü. Ö. Köylü, G. M. Faeth, "Radiative Properties of Flame-Generated Soot", *J. Heat Transfer* **115** (1993), no. 2, p. 409-417.

[19] T. L. Farias, Ü. Ö. Köylü, M. d. G. Carvalho, "Range of validity of the Rayleigh—Debye-–Gans theory for optics of fractal aggregates", *Appl. Opt.* **35** (1996), no. 33, p. 6560-6567.

[20] R. A. Dobbins, C. M. Megaridis, "Morphology of flame-generated soot as determined by thermophoretic sampling", *Langmuir* **3** (1987), no. 2, p. 254-259.

[21] Ü. Ö. Köylü, C. S. McEnally, D. E. Rosner, L. D. Pfefferle, "Simultaneous measurements of soot volume fraction and particle size/microstructure in flames using a thermophoretic sampling technique", *Combust. Flame* **110** (1997), no. 4, p. 494-507.

[22] M. Kholghy, M. Saffaripour, C. Yip, M. J. Thomson, "The evolution of soot morphology in a laminar coflow diffusion flame of a surrogate for Jet A-1", *Combust. Flame* **160** (2013), no. 10, p. 2119-2130.

[23] M. L. Botero, N. Eaves, J. A. H. Dreyer, Y. Sheng, J. Akroyd, W. Yang, M. Kraft, "Experimental and numerical study of the evolution of soot primary particles in a diffusion flame", *Proc. Combust. Inst.* **37** (2019), no. 2, p. 2047-2055.

[24] B. Konsur, C. M. Megaridis, D. W. Griffin, "Fuel preheat effects on soot-field structure in laminar gas jet diffusion flames burning in 0-g and 1-g", *Combust. Flame* **116** (1999), no. 3, p. 334-347.

[25] D. L. Urban, Z.-G. Yuan, P. B. Sunderland, G. T. Linteris, J. E. Voss, K.-C. Lin, Z. Dai, K. Sun, G. M. Faeth, "Structure and soot properties of nonbuoyant ethylene/air laminar jet diffusion flames", *AIAA J.* **36** (1998), no. 8, p. 1346-1360.

[26] J.-M. Citerne, H. Dutilleul, K. Kizawa, M. Nagachi, O. Fujita, M. Kikuchi, G. Jomaas, S. Rouvreau, J. L. Torero, G. Legros, "Fire safety in space - Investigating flame spread interaction over wires", *Acta Astronaut.* **126** (2016), p. 500-509.

[27] A. Guibaud, J.-M. Citerne, J.-L. Consalvi, G. Legros, "Pressure Effects on the Soot Production and Radiative Heat Transfer of Non-Buoyant Laminar Diffusion Flames Spreading in Opposed Flow over Insulated Wires", *Combust. Flame* **222** (2020), p. 383-391.

[28] J.-L. Consalvi, A. Guibaud, A. Coimbra, J.-M. Citerne, G. Legros, "Effects of oxygen depletion on soot production, emission and radiative heat transfer in opposed-flow flame spreading over insulated wire in microgravity", *Combust. Flame* **230** (2021), article no. 111447.

[29] J. Lawton, "Electrical aspects of combustion", *Clarenton* (1969).

[30] S. Karnani, D. Dunn-Rankin, "Detailed characterization of DC electric field effects on small non-premixed flames", *Combust. Flame* **162** (2015), no. 7, p. 2865-2872.

[31] F. B. Carleton, F. J. Weinberg, "Electric field-induced flame convection in the absence of gravity", *Nature* **330** (1987), no. 6149, p. 635-636.

[32] M. Belhi, P. Domingo, P. Vervisch, "Direct numerical simulation of the effect of an electric field on flame stability", *Combust. Flame* **157** (2010), no. 12, p. 2286-2297.

[33] J. Hu, B. Rivin, E. Sher, "The effect of an electric field on the shape of co-flowing and candle-type methane–air flames", *Exp. Therm. Fluid Sci.* **21** (2000), no. 1-3, p. 124-133.

[34] H. Schlichting, J. Kestin, *Boundary layer theory*, vol. 121, Springer, 1961.

[35] A. Guibaud, J.-M. Citerne, J.-L. Consalvi, O. Fujita, J. L. Torero, G. Legros, "Experimental evaluation of flame radiative feedback: methodology and application to opposed flame spread over coated wires in microgravity", *Fire Technol.* **56** (2020), no. 1, p. 185-207.

[36] K. R. Sacksteder, "The implication of experimentally controlled gravitational accelerations for combustion science", *Proc. Combust. Inst.* **23** (1991), no. 1, p. 1589-1596.

[37] L. Xie, T. Kishi, M. Kono, "Investigation on the effect of electric fields on soot formation and flame structure of diffusion flames", *Proc. Combust. Inst.* **24** (1992), no. 1, p. 1059-1066.

[38] P. J. Mayo, F. J. Weinberg, "On the size, charge and number-rate of formation of carbon particles in flames subjected to electric fields", *Proc. R. Soc. Lond., Ser. A* **319** (1970), no. 1538, p. 351-371.

[39] A. B. Fialkov, "Investigations on ions in flames", *Prog. Energy Combust. Sci.* **23** (1997), no. 5-6, p. 399-528.

[40] H. F. Calcote, D. B. Olson, D. G. Keil, "Are ions important in soot formation?", *Energy Fuels* **2** (1988), no. 4, p. 494-504.

[41] T. A. Sipkens, S. N. Rogak, "Technical note: Using k-means to identify soot aggregates in transmission electron microscopy images", *J. Aerosol Sci.* **152** (2021), article no. 105699.

[42] G. Legros, A. Fuentes, S. Rouvreau, P. Joulain, B. Porterie, J. L. Torero, "Transport mechanisms controlling soot production inside a non-buoyant laminar diffusion flame", *Proc. Combust. Inst.* **32** (2009), no. 2, p. 2461-2470.

[43] Z. Li, L. Qiu, X. Cheng, Y. Li, H. Wu, "The evolution of soot morphology and nanostructure in laminar diffusion flame of surrogate fuels for diesel", *Fuel* **211** (2018), p. 517-528.

[44] M. L. Botero, Y. Sheng, J. Akroyd, J. Martin, J. A. H. Dreyer, W. Yang, M. Kraft, "Internal structure of soot particles in a diffusion flame", *Carbon* **141** (2019), p. 635-642.

[45] B. R. Stanmore, J.-F. Brilhac, P. Gilot, "The oxidation of soot: a review of experiments, mechanisms and models", *Carbon* **39** (2001), no. 15, p. 2247-2268.

[46] Ü. Ö. Köylü, G. M. Faeth, "Optical Properties of Soot in Buoyant Laminar Diffusion Flames", *J. Heat Transfer* **116** (1994), no. 4, p. 971-979.

[47] L. Liu, M. I. Mishchenko, W. P. Arnott, "A study of radiative properties of fractal soot aggregates using the superposition T-matrix method", *J. Quant. Spectrosc. Radiat. Transfer* **109** (2008), no. 15, p. 2656-2663.

[48] M. Altenhoff, S. Aßmann, C. Teige, F. J. T. Huber, S. Will, "An optimized evaluation strategy for a comprehensive morphological soot nanoparticle aggregate characterization by electron microscopy", *J. Aerosol Sci.* **139** (2020), article no. 105470.

[49] D. Lottin, D. Ferry, J.-M. Gay, D. Delhaye, F.-X. Ouf, "On methods determining the fractal dimension of combustion aerosols and particleclusters", *J. Aerosol Sci.* **58** (2013), p. 41-49.

[50] P. M. Anderson, H. Guo, P. B. Sunderland, "Repeatability and reproducibility of TEM soot primary particle size measurements and comparison of automated methods", *J. Aerosol Sci.* **114** (2017), p. 317-X326.

[51] B. Zhao, Z. Yang, J. Wang, M. V. Johnston, H. Wang, "Analysis of soot nanoparticles in a laminar premixed ethylene flame by scanning mobility particle sizer", *Aerosol Sci. Technol.* **37** (2003), no. 8, p. 611-620.

[52] G. Bushell, R. Amal, J. Raper, "The effect of polydispersity in primary particle size on measurement of the fractal dimension of aggregates", *Part. Part. Syst. Charact.* **15** (1998), no. 1, p. 3-8.

[53] J. Y. Yin, L. H. Liu, "Influence of complex component and particle polydispersity on radiative properties of soot aggregate in atmosphere", *J. Quant. Spectrosc. Radiat. Transfer* **111** (2010), no. 14, p. 2115-2126.

[54] N. Doner, F. Liu, "Impact of morphology on the radiative properties of fractal soot aggregates", *J. Quant. Spectrosc. Radiat. Transfer* **187** (2017), p. 10-19.

[55] Ü. Ö. Köylü, G. M. Faeth, T. L. Farias, M. d. G. Carvalho, "Fractal and projected structure properties of soot aggregates", *Combust. Flame* **100** (1995), no. 4, p. 621-633.

[56] K. Adachi, S. H. Chung, H. Friedrich, P. R. Buseck, "Fractal parameters of individual soot particles determined using electron tomography: Implications for optical properties", *J. Geophys. Res. Atmos.* **112** (2007), no. D14.

[57] A. Guibaud, J.-M. Citerne, J. M. Orlac'h, O. Fujita, J.-L. Consalvi, J. L. Torero, G. Legros, "Broadband modulated absorption/emission technique to probe sooting flames: Implementation, validation, and limitations", *Proc. Combust. Inst.* **37** (2019), no. 3, p. 3959-3966.

[58] J.-B. Renard, M. Francis, E. Hadamcik, D. Daugeron, B. Couté, B. Gaubicher, M. Jeannot, "Scattering properties of sands. 2. Results for sands from different origins", *Appl. Opt.* **49** (2010), no. 18, p. 3552-3559.

[59] A. Guibaud, J.-L. Consalvi, J. M. Orlac'h, J.-M. Citerne, G. Legros, "Soot production and radiative heat transfer in opposed flame spread over a polyethylene insulated wire in microgravity", *Fire Technol.* **56** (2020), no. 1, p. 287-314.